Sedimentary structure derived from multi-mode ambient noise tomography with dense OBS network at the Japan Trench

Lina Yamaya[1], Kimihiro Mochizuki[1], Takeshi Akuhara[1], Kiwamu Nishida[1]

[1]Earthquake Research Institute, University of Tokyo, Tokyo, 113-0023, Japan

Correspondence to: Lina Yamaya (lina@eri.u-tokyo.ac.jp)

Abstract. We derive the 3-D S-wave velocity structures of sediments and upper crust in the region off Ibaraki at Japan Trench subduction zone by applying ambient noise tomography to a dense array of short-period ocean bottom seismometers (OBSs). The cross-spectra were calculated using 27- or 142-day continuous seismic data, and the phase velocities of the fundamental and the first-higher Rayleigh wave modes are obtained in the frequency ranges of 0.1–0.25 Hz and 0.17–0.3 Hz, respectively. Our 1-D S-wave velocity inversion based on the trans-dimensional Markov chain Monte Carlo method revealed multiple sedimentary layers above the acoustic basement and the upper crustal structure. The 1-D structure was then used as a reference model to conduct ambient noise tomography and non-linear inversion of the 3-D S-wave velocity structure by collecting data of the local 1-D S-wave velocity structure. Our 3-D S-wave velocity structure revealed three main points: (1) The acoustic basement is situated at a depth of ~4 km depth; (2) the crustal structure is more complex than that of the sedimentary layers; and (3) the southern region has a complex crustal structure in which subducting seamounts were identified by previous P-wave velocity tomographies.

1 Introduction

Ocean bottom seismometer (OBS) networks of both temporary and permanent deployment have been recently developed along subduction zones (e.g., Cascadia Initiative: Toomey et al., 2014; DONET: Kaneda et al., 2015; S-net: Kanazawa et al., 2016). High-frequency waveform data from OBSs, most of which were obtained at frequencies higher than 0.1 Hz, can be used in receiver function analysis for evaluating shallow subduction structures (e.g., Reeves et al., 2015; Akuhara and Mochizuki, 2015) or waveform modeling to determine seismic source properties (e.g., Nakano et al., 2015; Takemura et al., 2020). Such studies help us to better understand the lithology, deformation, and earthquake processes of subduction zones. However, uncertainties in shallow thick sedimentary structures could bias the estimates of deeper structures and source locations owing to a trade-off between seismic velocity and depth. Intense reverberations within the sediment can also distort these estimates (e.g., Audet 2016). Thus, constraining the sedimentary structure is essential for addressing these limitations. Moreover, understanding heterogeneous structure within the sediments and the upper most crusts can give better constraints on local deformation processes due to subduction of rough topographies such as seamounts (e.g., Ruh et al., 2016; Sun et al., 2020). Although active-source methods have been widely used for studying sedimentary structures (e.g., Tsuru et al., 2002),

conducting 3-D surveys is cost prohibitive. Although ambient noise tomography is an alternative tool that does not have the active-source requirement (Bussat and Kugler, 2011), its potential has not been fully explored.

This method has been widely used during the past decade to derive seismic structures (e.g., Shapiro et al., 2005). The basic principle of ambient noise seismic interferometry dates back to the pioneering work of Aki (Aki, 1957). Ambient noise tomographies reveal S-wave velocity structures using dispersion curves of surface-wave phase velocities (e.g., Lin et al., 2008; Ekström et al., 2009) or group velocities (e.g., Shapiro et al., 2005) calculated from cross-correlations of seismic noise data. Many studies have used onshore stations to show tomographic images of S-wave velocity structures of the crust and the uppermost mantle at the regional scale (e.g., Yang et al., 2008; Sun et al., 2010; Calkins et al., 2011; Bao et al., 2015) or the global scale (e.g., Nishida et al., 2009). More recently, dense seismic arrays have been used for imaging local-scale structures of the shallow crust (e.g., Wang et al., 2017).

For offshore regions, few ambient noise studies have used high-frequency data because the low S-wave velocity of thick sedimentary layer increases the wave number between stations, which creates strong attenuation. Most studies have analyzed data in periods ranging from several to dozens of seconds using data from broadband OBSs with station intervals of tens to hundreds of kilometers. Since Lin et al. (2006) suggested the possibility of ambient noise tomography across oceans, studies have resolved the seismic velocity structure of the crust and the uppermost mantle (e.g., Zha et al., 2014; Ball et al., 2016; Corela et al., 2017; Ryberg et al., 2017; Hable et al., 2019). For the regional scale, 1-D imaging of an oceanic lithosphere–asthenosphere system has been derived from ambient noise seismic interferometry applied to data from broadband OBSs (e.g., Harmon et al., 2007; Takeo et al., 2013; Lin et al., 2016).

Recently, few studies have imaged the high-resolution sedimentary and the upper most crustal structures beneath seafloor using ambient noise. Bussat and Kugler (2011) derived the structures of the sediments and the upper crust using data in several frequencies obtained from a super-dense OBS array with a station interval of about 500 m. Other than OBS arrays, Mordret et al. (2013, 2014) used an ocean-bottom cable array with a station interval of several meters in an oil industrial field and resolved the shallow sedimentary structure to a depth of 700 m below sea level, within an area of ~10 × 10 km^2. As for Japan trench, frequency–wavenumber analysis of ambient noise recorded by distributed acoustic sensing (DAS) became also feasible for revealing high-resolution 2-D shallow structures at off Sanriku region (e.g., Spica et al., 2020), although this method is not based on seismic interferometry. Despite the importance of 3-D high-resolution structures, few studies have resolved local-scale tomographic structures including sedimentary layers by using short-period OBSs with station intervals of less than 10 km.

This study targets off the Ibaraki region, northeastern Japan at Japan Trench subduction zone. This region coincides with the southern boundary of the focal region of the 2011 off the Pacific coast of Tohoku Earthquake (the 2011 Tohoku-oki earthquake) where a subducted seamount of the size of ~50 km wide and ~3 km high has been identified at a depth of ~10 km (Mochizuki et al., 2008). The influence by the tectonic processes of the seamount subduction on the seismic rupture propagations has been discussed (e.g., Nakatani et al., 2015). Detailed structure within the overriding plate is needed to better understand the tectonic processes by the seamount subduction.

In this study, we measure the phase velocities of the fundamental and the first-higher modes of Rayleigh wave and derive the S-wave velocity structure of the sedimentary layers and the upper crust. Although surface-wave inversion often suffers from a trade-off between the estimation of the layer thickness and that of S-wave velocity in the model obtained by surface-wave non-linear inversion, using both the fundamental and the first-higher modes provides a better constraint on both the layer thickness and that of S-wave velocity structure because of the different sensitivities between these two modes. The obtained S-wave velocity resolves multiple layers above the acoustic basement. The results indicate relatively heterogeneous features in the southern part of the array, which may be resulted from the subducted seamount. The obtained high-resolution structures will make a significant contribution to waveform modeling of OBS data (e.g., waveform inversion and receiver-function analysis), which will enable us to resolve better S-wave velocity structures in deeper parts or to determine accurate earthquake source mechanisms reflecting the present state of the stress around the subducted seamount.

2 Study area and data

This study used data from a dense array with 30 OBSs deployed off the Ibaraki region in northeastern Japan along the Japan Trench subduction zone (Figure 1). The Pacific plate is subducting beneath the northeastern Japan from the east. Offshore seismic surveys at the forearc have identified a strong unconformity at ~1–3km depth beneath the seafloor, which is interpreted as the top of the Cretaceous sediments (e.g., Tsuru et al., 2002; Takahashi et al. 2004). The consolidated Cretaceous sediments have S-wave velocities of ~2.5 km/s, whereas the unconsolidated sediments above this unconformity have S-wave velocities of less than ~1 km/s. (e.g., Spica et al., 2020). Therefore, the top of the Cretaceous sediments constitutes the acoustic basement. The OBS array lies over the continental slope at the southern end of the Japan trench, where the top of the subducting Pacific plate is revealed at 10–15 km (Mochizuki et al., 2008; Nakahigashi et al., 2012). A chain of seamounts exists on the incoming Pacific plate seaward of the trench (Figure 1, inset). Mochizuki et al. (2008) showed that a large seamount of the size of ~50 km wide and ~3 km high is being subducted beneath the southern part of the dense OBS array. The bathymetric depression seen in this southern part reflects the seamount subduction, whereas the seafloor topography appears to be fairly flat to the north. Within the array, active-source seismic surveys have revealed that small-scale (<20 km) lateral variations in the topographiy of the acoustic basement and the upper crust. The seamount subduction may cause such structural variations while the seamount itself is located ~5 km deeper (e.g., Sun et al., 2020). Mochizuki et al. (2008) also argued that a large seamount might affect repeating M~7 earthquakes with a fairly constant recurrence interval (~20 years) at the frontal region of its subduction (e.g., Matsumura, 2010). To discover a more detailed structure of the subducting seamount or the relationship between the subducting seamount and its earthquake activity, the OBS array was deployed.

Six months after the starting of the observation (October 2010), the 2011 Tohoku-oki earthquake occurred. This study region lies at the southern end of the focal area of the Tohoku-oki earthquake and 300 km south of its epicenter. The largest aftershock (Mw 7.8) occurred 30 min after the mainshock in the landward side of the array. More than 10,000 aftershocks that occurred just beneath the network were observed (Nakatani et al., 2015). Shinohara et al. (2011, 2012) conducted offshore aftershock

observations and found that most aftershocks occurred at the plate boundary, but some of them occurred in the upper-most crust. Recent studies have reported slow earthquake activities in the southern end of the region (e.g., Nishikawa et al., 2019). The OBS array is composed of 35 three-component short-period (1 Hz) seismometers (LE-3Dlite, Lennartz, Germany) with a station interval of approximately 6 km. First, 24 OBSs near the array center were deployed on October 17, 2010, and the surrounding 11 OBSs were added on February 14, 2011. Of these, 31 were successfully recovered by September 2011 (Nakatani et al., 2015). An active-source seismic survey was conducted during the observation, the results of which were used to determine the horizontal sensor orientation. The data from two OBSs were excluded. In the first case, the OBS missed seismic records from air-gun shots, and the amplitude level of the second OBS was found to be erroneously low, owing likely to a malfunction of its recorder.

During the observation period, the Mw 7.3 Sanriku-oki earthquake occurred on March 9, 2011, and was followed by the Mw 9.0 Tohoku-oki earthquake occurring on March 11, 2011. Many aftershocks followed these earthquakes. Ambient noise tomography requires an assumption of the isotropic and homogeneous source distribution in theory (e.g., Wapenaar, 2004). Because the intense aftershock activity breaks this assumption, we used data obtained before the Sanriku-oki earthquake. We analyzed only the vertical and radial components to measure phase velocities of Rayleigh wave. We did not use transverse components to measure phase velocities of Love wave because the variance reduction of the transverse component for higher frequencies (0.15Hz–) was insufficient to measure phase velocities like section 4.1. Love wave is extremely sensitive to the heterogeneity in the top sediments with very low S-wave velocities (~0.05 km/s), which breaks the assumption of the 1-D structure averaged in the array. Therefore, our dataset consisted of vertical and radial components of 20 OBSs for 142 days, vertical and radial components of nine OBSs for 22 days, and a vertical component of an OBS for 142 days.

3 Ambient noise interferometry: calculation of cross-spectra

In sections 3–6, the four steps of the analytic process are discussed, as illustrated in Figure 2: (1) calculation of the cross-spectra, (2) measurement of the phase velocities assuming a 1-D structure for inversion of the reference 1-D S-wave velocity structure, (3) measurement of the phase-velocity anomalies for inversion of the 2-D phase-velocity structure, and (4) inversion of the 3-D S-wave velocity structure by combining local 1-D S-wave velocity structures at every OBS station.

We applied a band-pass filter of 0.05–9.0 Hz to the data and decimated data from 200 to 20 Hz. We found that the ambient noise data of frequencies higher than about 0.1 Hz were usable after deconvolving the data using the instrumental response function. We did not use data of lower frequencies than about 0.1 Hz were because of the low sensitivity of the short-period sensors. Note that this frequency range (0.1 Hz–) of ambient noise data is not strongly contaminated with the tilt noise (e.g., Tian & Ritzwoller, 2017). After deconvolving the data using the instrumental response function, we divided all data records into 10-min segments and removed linear trends. We discarded segments with contamination of transients (e.g., glitches or instrumental noise) from the dataset and applied one-bit normalization (e.g., Bensen et al., 2007) to suppress the effects of

non-stationary phenomena such as earthquakes. One-bit normalization is a powerful and simple tool when used to observe ambient noise that still contains small earthquakes after removing many aftershocks and earthquake-like signals.

The observed power of ambient noise can also vary in the frequency domain. We calculated the Fourier spectra for all 10-min segments with spectrum whitening (e.g., Bensen et al., 2007) to suppress temporal changes in the frequency content of the microseisms. We then calculated the cross-spectra for each station pair p and each component γ as

$$\rho_{p,\gamma}^{\mathrm{obs}}(\omega) = \frac{f_{i,\gamma}(\omega) \cdot \bar{f}_{j,\gamma}(\omega)}{\left|f_{i,\gamma}(\omega)\right|\left|\bar{f}_{j,\gamma}(\omega)\right|}, \tag{1}$$

where $f_{i,\gamma}$ is the Fourier spectrum of one-bit normalized data for the i-th station, and the overline represents the complex conjugate. The value γ takes either the radial R component or the vertical Z component. We applied this convention throughout the study.

Cross-correlation functions (CCFs), which are calculated by using the inverse Fourier transform of the cross-spectra, are dominated by Rayleigh wave (Figure 3). The fundamental mode of Rayleigh wave clearly appeared in the vertical component in the frequency range of 0.0625–0.3125 Hz (Figure 3a, c). The fundamental and the first-higher modes of Rayleigh wave appeared in the radial component (Figure 3b, d). This tendency is consistent with previous studies (e.g., Savage et al., 2013). For both modes, CCFs from 0.0625 Hz to 0.1875 Hz indicate higher phase velocities than those from 0.1875 Hz to 0.3125 Hz. In our calculations, a positive (negative) lag time of a CCF indicates Rayleigh waves from the northwest (southeast). Some CCFs showed larger Rayleigh-wave amplitudes in the negative lag times than those in the positive lag time, which means that more ambient noise traveled from the Pacific Ocean, where the dominant sources exist (e.g., Takagi et al., 2018).

4 1-D reference seismic velocity structure

In this section, we discuss two steps for performing inversion of the 1-D reference seismic velocity structure. First, we measured the dispersion curves of Rayleigh waves averaged in the region of the array using the spatial auto-correlation (SPAC) method (Aki, 1957; Nishida et al., 2008; Haney et al., 2012). Then, we performed inversion of the 1-D S-wave velocity structure using the trans-dimensional Markov chain Monte Carlo (MCMC) method (Bodin et al., 2012).

4.1 Measurement of dispersion curves of Rayleigh waves

We used the SPAC method to measure the phase velocities as a function of frequencies (e.g., Nishida et al., 2008; Takeo et al., 2013) rather than frequency-time analysis (FTAN: e.g., Levshin et al., 1989). FTAN is one of the traditionally and commonly used method. Since this method directly measures the dispersion curve of each station pair, it is suitable when the cross-correlation functions have clear peaks. Many studies using sparse arrays have applied this method to ambient noise tomographies (e.g., Bensen et al., 2008). However, it is difficult to apply this method to a heterogeneous medium, because it causes complex shapes of cross-correlation functions by strong dispersions, multimode overlaps and scattering.

Even in a case of complex shapes of cross-correlation functions, a two-step measurement based on the SPAC method is feasible for the phase-arrival measurements practically when the dense array data are available. This method makes the reference 1-D structure averaged in the target region using all station pairs in the first step (e.g., Nishida et al., 2008; Takeo et al., 2013). In the next step, this method measures perturbations for each station pair from the reference 1-D structure. This two-step method is optimal in which the phase arrivals cannot be identified due to strongly heterogeneous or dispersive structure (e.g., volcano: Nagaoka et al., 2012; oceanic basin: Takeo et al., 2013) or multi-mode overlapping (Nishida et al., 2008).

In the SPAC method, for the vertical component ($\gamma = \mathrm{Z}$), the synthetic cross-spectrum at an angular frequency ω assuming a local 1-D seismic velocity structure beneath the entire area of the OBS array can be expressed as

$$\rho_Z^{\mathrm{syn}}\left(d_p, a_Z, c^{1\mathrm{D}}; \omega\right) = a_Z(\omega) J_0\left(\frac{\omega d_p}{c^{1\mathrm{D}}(\omega)}\right), \tag{2}$$

Where a_Z is the power spectrum for vertical component, d_p is the station interval for p-th pair, $c^{1\mathrm{D}}$ is the assumed phase velocity averaged in the region of the array, and J_0 is the zeroth-order Bessel function of the first kind. In this study, following Nagaoka et al. (2012), Q values are ignored because the size of our array is sufficiently small. For the radial components ($\gamma = R$), if a wavelength is considerably shorter than its station interval, we can neglect the contribution of Love waves (e.g., Takeo et al., 2013). With this assumption, the synthetic cross-spectrum can be written as

$$\rho_R^{\mathrm{syn}}\left(d_p, a_R, c^{1\mathrm{D}}; \omega\right) = a_R(\omega)\left[J_0\left(\frac{\omega d_p}{c^{1\mathrm{D}}(\omega)}\right) - J_1\left(\frac{\omega d_p}{c^{1\mathrm{D}}(\omega)}\right) \Big/ \left(\frac{\omega d_p}{c^{1\mathrm{D}}(\omega)}\right)\right], \tag{3}$$

where J_1 is the first-order Bessel function of the first kind.

We measured the phase velocity at a fixed angular frequency for the entire area by maximizing the variance reduction as

$$VR\left(a_\gamma, c^{1D}; \omega\right) = 1 - \frac{\Delta_\gamma\left(a_\gamma, c^{1\mathrm{D}}; \omega\right)}{\sum_p w_p\left[\rho_{p,\gamma}^{\mathrm{obs}}(\omega)\right]^2}, \tag{4}$$

where the squared difference $\Delta_\gamma(a, c^{1\mathrm{D}}; \omega)$ between the synthetic (equations (2) or (3)) and observed cross-spectra (equation (1)) is written as

$$\Delta_\gamma\left(a_\gamma, c^{1\mathrm{D}}; \omega\right) = \sum_p w_p\left[\rho_{p,\gamma}^{\mathrm{obs}}(\omega) - \rho_\gamma^{\mathrm{syn}}\left(d_p, a_\gamma, c^{1\mathrm{D}}; \omega\right)\right]^2. \tag{5}$$

Here, w_p is a weighting term set to the reciprocal of the square root of the station distance. We found that this choice offers sharp resolution for the phase velocity, whereas it caused side lobes with relatively large amplitudes. We used only the real part of the observed cross-spectrum because the imaginary part reflects mainly the heterogeneity of the noise sources (e.g., Weaver et al., 2009).

Figure 4c–d shows the variance reduction (equation 5) against frequency and phase velocity. To obtain this diagram, we fixed a_γ at a value stratifying $\frac{\partial \Delta}{\partial a} = 0$ at each angular frequency ω. Since a is a function of ω, this a minimizes Δ analytically (e.g., Nagaoka et al., 2012). The fundamental mode of Rayleigh waves was clearly found in the vertical and the radial components, whereas the first-higher mode was identifiable only in the radial components. We note that the array geometry on regular grids

(Figure 1) caused a checkerboard artifact in the variance reduction above 0.15 Hz, particularly in the radial component (Figure 4d). The sparse distribution of data along the distance (i.e., station interval) axis makes it difficult to constrain zero-crossings of the cross-spectrum (Figure 4a, b). Nevertheless, we can choose the appropriate mode branch in the following manner.

We first measured the phase velocity that maximizes the variance reduction at the highest frequency (0.25 Hz for the fundamental mode and 0.3 Hz for the first-higher mode). Then, for subsequent lower frequencies, we searched for the phase velocities that maximize the variance reduction in the vicinity of the phase velocity at the previous frequency. The resulting phase velocity range of the fundamental mode was 0.5–2.4 km/s at 0.1–0.25 Hz, and that of the first-higher mode was 0.8–1.5 km/s at 0.17–0.3 Hz, as represented by white dots in Figure 4c, d. Following Takeo et al. (2013), we estimated the uncertainties of the phase velocities using a bootstrap method (Efron, 1992). We randomly selected station pairs allowing for overlapping and made 100 sets of bootstrap samples. We measured the phase velocities using these bootstrap samples and estimated the measurement errors, which varied from 1.0×10^{-5} to 0.83.

We used the vertical component to measure the phase velocities of the fundamental mode of Rayleigh wave and the radial component to measure those of the first-higher mode. Since previous studies suggested that the ellipticity (horizontal to vertical amplitude ratio) of higher-mode Rayleigh wave particle motion is high when the region typically has thick sediments beneath the seafloor (e.g., Savage et al., 2013 : see section 8 for details), we measured the first-higher mode using the radial component. The higher variance reduction of the radial component for the first-higher mode agrees with the previous studies.

The radial component is potentially contaminated by Love wave when a wavelength is comparable to or longer than the station interval (Aki, 1957); however, we obtained similar results for the fundamental mode at low frequencies when using the radial component. This consistency suggests that the effect of Love wave was not significant. This justified the use of the radial component for the higher mode, which also had shorter wavelengths than the station intervals, similar to those of the fundamental mode.

4.2 Inversion for 1-D S-wave velocity structure

We used the trans-dimensional MCMC method to perform inversion for the averaged 1-D S-wave velocity structure beneath the OBS array. We set a prior probability distribution of the parameters (number of layers, interface depth, and S-wave velocity of each layer) as a uniform distribution with sufficiently wide bounds to be regarded as non-informative (1–10 for the number of layers; 2.3–10 km for interface depths; and 0.1–5 km/s for S-wave velocities). Although the phase velocities of Rayleigh waves are sensitive to the seafloor depth (Figure S1), we fixed the value at 2.3 km, which is the average depth in this array. We included the effect of seafloor depth in the 3-D structure inversion analysis (section 6). We did not solve for P-wave velocities and densities; rather, we fixed them using the empirical scaling law by equations (1) and (9) in Brocher (2005). Although this scaling law does not consider unconsolidated sediments, the predicted P-wave velocity from very low S-wave velocity (~0.3 km/s, which is the lowest S-wave velocity of Spica et al., 2020) is ~1.5 km/s, which is consistent with P-wave velocity structures obtained by active-source surveys at off Ibaraki region (e.g., Tsuru et al., 2002) or by Ocean Drilling Program at Japan Trench off northeast Japan (Shipboard Scientific Party, 2000). We ignored Q values, assuming perfect elastic

medium as noted above. The S-wave velocity of the bottom layer was fixed at 4.6 km/s as the typical value of the S-wave velocity at the upper mantle because the bottom layer was sufficiently deep for our Rayleigh-wave inversion analysis.

The inversion began with a randomly generated velocity model. At each iteration, the model from the previous iteration is slightly modified by either adding a layer, removing a layer, perturbing the S-wave velocity of a layer, or moving the bottom depth of a layer. Then, the synthetic dispersion curves were calculated using the method of Saito (1988) to evaluate the likelihood, which is defined in the form of multivariate Gaussian distribution with a diagonal covariance matrix for data error (e.g., Bodin et al. 2012). The standard deviations, or the diagonal elements, were set to a uniform value of 0.1 km/s, which was determined ad hoc. Finally, the model was judged to accept or not by the Metropolis–Hastings–Green criterion (Green, 1995). We repeated this iteration 500,000 times, but we did not save the models during the first 100,000 iterations. Afterward, we saved the models at every 100 iterations. We employed a parallel tempering algorithm to enhance the capability of global sampling, which involved 20 non-tempered and 80 tempered MCMC chains (e.g., Sambridge, 2014). We obtain 10,000 models after the inversion, which were used to construct posterior probability distribution and related quantities such as marginal distribution.

The obtained posterior probability distribution suggests that the region shallower than 4 km is well constrained despite the given loosely bounded uniform priors (Figure 5a–c). The median model showed a very low-velocity layer (layer 1) immediately beneath the seafloor and another low-velocity layer (layer 2) beneath the first. The thicknesses of layer 1 and layer 2 were 0.4 km and 1.4 km, and their S-wave velocities were 0.34 km/s and 0.85 km/s, respectively. Below these layers, the S-wave velocity sharply increased to 2.1 km/s at ~4 km in depth, which suggests the depth of the acoustic basement. This depth is consistent with 2-D reflection surveys (Tsuru et al., 2002; Nishizawa et al., 2009) and P-wave velocity tomography using data from an active-source survey (Mochizuki et al., 2008).

We also obtained a low-velocity layer with an S-wave velocity of 2.1 km/s (layer 3) just beneath the acoustic basement, although the marginal distribution indicated large uncertainty compared with layers 1 and 2. The thickness of layer 3 was ~1.2 km. Beneath that layer, the S-wave velocity gradually increased to more than 3 km/s, which is consistent with the S-wave velocity of the upper crust. One concern is that the phase velocity of the first-higher mode may not be well constrained at higher frequencies than 0.25 Hz, as implied by relatively low variance reduction (Figure 4d). We hence conducted the same inversion analysis without these high-frequency data (Figure S2). The results show no critical difference with or without the high-frequency data, which suggests the robustness of our analysis.

5. 2-D Phase velocity map

In this section, we measured path-averaged phase-velocity perturbations relative to the reference phase velocity obtained in section 4.1. In the next step, we invert these phase-velocity perturbations for the 2-D map of the phase velocities in each frequency range.

First, we measured the path-averaged phase velocity perturbation with respect to the reference 1-D phase velocity for each station pair. Following Nagaoka et al. (2012), we inferred the phase velocity perturbation by fitting the synthetic cross-spectrum $\rho'^{\mathrm{syn}}_{p,\zeta}$ to the observed cross-spectrum $\rho^{\mathrm{obs}}_{p,\gamma}(\omega)$ for each path and for each frequency binned by 0.025 Hz with 0.0125 Hz overlap. The central angular frequency of the l-th bin for the fundamental mode ($\zeta = 0$) is given by

$$\omega_0^l = 2\pi(0.0125 \times\ l + 0.1) \quad (l = 1, 2, \dots, 12), \tag{6}$$

and that for the first-higher mode ($\zeta = 1$) is written as

$$\omega_1^l = 2\pi(0.0125\ \times l + 0.175) \quad (l = 1, 2, \dots, 6). \tag{7}$$

From these equations, we used the central frequency for referring to each frequency bin.

First, we used the vertical component to measure the phase velocities of the fundamental mode of Rayleigh wave because the CCFs of this component mostly have signals of the fundamental mode of Rayleigh wave only. The synthetic cross-spectrum of the fundamental mode including the phase velocity perturbation of each station pair $\rho'^{\mathrm{syn}}_{p,0}(b, e_0^l; \omega)$ is given by

$$\rho'^{\mathrm{syn}}_{p,0}(b, e_0^l; \omega) = b_p(\omega_0^l)\rho_Z^{\mathrm{syn}}\left(d_p, a_Z, (1 + e_0^l)c_0^{1\mathrm{D}}; \omega\right), \tag{8}$$

where b_p is the correction of the power spectrum for each path and for each angular frequency bin, e_0^l is the assumed phase-velocity perturbation at the l-th frequency bin, and $c_0^{1\mathrm{D}}$ is the reference phase velocity of the fundamental mode of Rayleigh wave measured in section 4.1. ρ_Z^{syn} is defined in equation (5). We calculated the misfit function $\Delta'_{p,\zeta,l}\left(b, e_\zeta^l;\ \omega_\zeta^l\right)$ as

$$\Delta'_{p,\zeta,l}\left(b, e_\zeta^l; \omega_\zeta^l\right) = \int_{\omega_\zeta^l - 2\pi\cdot 0.0125}^{\omega_\zeta^l + 2\pi\cdot 0.0125} \left[\rho^{\mathrm{obs}}_{p,\gamma}(\omega) - \rho'^{\mathrm{syn}}_{p,\gamma}\left(b_p, e_\zeta^l; \omega\right)\right]^2 d\omega \tag{9}$$

for each frequency bin and each assumed phase velocity perturbation e_0. We minimized the misfit function $\Delta'_{p,\gamma}\left(b_p, e_0; \omega\right)$ analytically with respect to b_p. Hence, grid search was necessary only for e_ζ^l.

To avoid cycle skipping, we searched for the phase velocity perturbation only when b was positive, and we limited the search range of the phase velocity perturbations in two steps. In the first step, we calculated the misfit function, Δ', starting with 0.15 Hz ($l = 4$) because the signal-to-noise ratio was best. Since the possibility of the cycle skipping is related to the station distance, we changed the search range of the velocity perturbation in accordance with the station distance, as shown in Table 1. In the next step, we measured the phase velocity perturbations for the adjacent lower and higher frequency bins. This time, we further narrowed the search range referring to the results from the previous bin (Table 2). When no local minimum was found, we stopped measuring the phase velocity perturbations in the frequency range and the subsequent frequency ranges for the corresponding pair.

Next, we measured the phase velocity perturbation of the first-higher mode of Rayleigh wave using the radial component. Since this component contains both signals of the fundamental and the first-higher modes (Figure 3b, d), we fixed $a_Z(\omega)$ and $a_R(\omega)$, which represent the power spectrum of the fundamental and the first-higher modes, respectively, at the values obtained during the analysis of section 3.1. The synthetic cross-spectrum is shown as

$$\rho'^{\mathrm{syn}}_{p,1}(b, e_1^l; \omega) = b_p(\omega_1^l)\left\{\rho_Z^{\mathrm{syn}}\left(d_p, a_Z, (1 + e_0^l)c_0^{1\mathrm{D}}; \omega\right) + \rho_R^{\mathrm{syn}}\left(d_p, a_R, (1 + e_1^l)c_1^{1\mathrm{D}}; \omega\right)\right\} \tag{10}$$

where e_1^l is the assumed phase velocity perturbation at the l-th frequency bin, $(1+e_0^l)c_0^{1\mathrm{D}}$ is the phase velocity of the fundamental mode of Rayleigh wave measured for each path above, and $c_1^{1\mathrm{D}}$ is the reference phase velocity of the first-higher mode of Rayleigh wave. Again, b_p was analytically determined. We used a similar procedure for the first-higher mode to search for the phase velocity perturbation; the only difference was that in the first step, we used $l = 1$ in the search range shown in Table 1.

For the fundamental mode of Rayleigh wave, the resultant ranges of phase velocity perturbation were -10% to +10% at 0.1125 Hz and -30% to +30% at 0.20–0.25 Hz (Figure 6a–c). For the first-higher mode, the results showed -20% to +20% variations in the phase-velocity perturbations at 0.1875–0.20 Hz and -30% to +30% at 0.2125–0.25 Hz (Figure 7a–c).

Next, to map the phase velocities in each frequency range, we conducted iterative non-linear inversion using the fast marching method (Rawlinson et al., 2005; Saygin, 2007), which solves the eikonal equation directly. We used a grid size of $0.032° \times 0.026°$, approximately 3 km × 3 km (Figure S3). We then minimized the objective function $S(\boldsymbol{m})$ for each frequency and for each mode of Rayleigh wave as

$$S(\boldsymbol{m}^{2\mathrm{D}}) = (\boldsymbol{g}(\boldsymbol{m}^{2\mathrm{D}}) - \boldsymbol{\phi})^T \boldsymbol{C}_d^{-1}(\boldsymbol{g}(\boldsymbol{m}^{2\mathrm{D}}) - \boldsymbol{\phi}) + \epsilon(\boldsymbol{m}^{2\mathrm{D}} - \boldsymbol{m}_0)^T \boldsymbol{C}_m^{-1}(\boldsymbol{m}^{2\mathrm{D}} - \boldsymbol{m}_0). \quad (11)$$

Here, $\boldsymbol{g}(\boldsymbol{m}^{2\mathrm{D}})$ is the predicted travel time for the model $\boldsymbol{m}^{2\mathrm{D}}$, and $\boldsymbol{\phi}$ is the observed travel time data calculated as

$$\phi_{p,\zeta}^l = \frac{d_p}{(1+e_\zeta^l)c_\zeta^{1\mathrm{D}}(\omega_\zeta^l)}, \quad (12)$$

for the p-th pair and ζ-th mode of Rayleigh wave, where $\boldsymbol{C}_d$ is the data covariance matrix, $\boldsymbol{C}_m$ is the model covariance matrix, $\boldsymbol{m}_0$ is the initial model, $\boldsymbol{m}^{2\mathrm{D}}$ is the predicted model, and ϵ is the damping parameter. Following Rawlinson et al. (2006), we fixed the damping parameters to be 200 for the frequency bins of 0.1125–0.1375 Hz, 500 for 0.15–0.1625 Hz, and 1,000 for 0.175–0.25 Hz for the fundamental mode (Figure S4a, b). For the first-higher mode, the damping factor was set to 200 irrespective of the frequency (Figure S4c). We did not apply the smoothing parameter owing to the array geometry on the regular grids. We used the reference phase velocities as initial models, and we iterated 10 times to obtain the final model.

We calculated the root-mean-square (RMS) data residual as

$$\mathrm{RMS} = \sqrt{\frac{|\boldsymbol{\phi} - \boldsymbol{g}(\boldsymbol{m}^{2\mathrm{D}})|^2}{N}}, \quad (13)$$

where N is the number of observed travel time data. The RMS was improved from 39.00 s for the initial 1-D model to 10.32 s for the final 2-D model. For the fundamental mode, a low-velocity anomaly was located at the northern side of the array at lower frequencies (Figure 6e, f), and two low-velocity anomalies were located at the northern side and central part at higher frequencies (Figure 6g, h). For the first-higher mode, a low-velocity anomaly was also located at the northern side at lower frequencies (Figure 7d), and a low-velocity was found in the central part at higher frequencies (Figure 7e, f). The western part had higher velocity at lower frequencies for both modes (Figure 6e, 7d).

Following Zha et al. (2014), we estimated the uncertainties of the phase velocities using a bootstrap method (Efron, 1992). We randomly sampled station pairs allowing for overlap and made 100 sets of bootstrap samples. We performed inversion of the

phase velocity maps using these bootstrap samples and estimated the measurement errors (Figure S5). The standard deviations of the fundamental mode of Rayleigh wave are generally less than 0.05 km/s, and those of the first-higher mode were mainly less than 0.1 km/s. Therefore, the uncertainties were less than 10% for both the fundamental and first-higher modes. We conducted the checkerboard test and confirmed that velocity anomalies with a ~10 km horizontal length can be recovered (Figures S6 and S7).

6. 3-D S-wave velocity structure

We next obtained the phase velocity maps of 12 (6) frequency bands for the fundamental (first-higher) mode of Rayleigh wave. We applied 1-D non-linear inversion (Herrmann, 2013) for each horizontal grid q at a given location with longitude and latitude to construct a 3-D S-wave velocity structure. For each horizontal grid q, we minimized the misfit function Δ_q as

$$\Delta_q = \sum_{l,\zeta} \frac{\left[c_q^{\mathrm{obs}}\left(\omega_\zeta^l\right) - c_q^{\mathrm{syn}}\left(\omega_\zeta^l, \boldsymbol{m}_{\mathrm{q}}^{\mathrm{3D}}\right)\right]^2}{C_q^{\mathrm{err}}\left(\omega_\zeta^l\right)^2}, \tag{14}$$

with respect to a given S-wave velocity model parameter $\boldsymbol{m}_{\mathrm{q}}^{\mathrm{3D}}$, where c_q^{obs} is the phase velocity for the q-th grid discussed in section 5, c_q^{syn} is the synthetic phase velocity for the model $\boldsymbol{m}_{\mathrm{q}}^{\mathrm{3D}}$, and c_q^{err} is the standard deviation of the phase velocities (Figure S5).

We created the initial model based on the median from the MCMC sampling (Figure 4). This initial model included three layers at the top with sharp velocity contrasts, corresponding to layers 1–3; below these layers, the velocity gradually increased with depth. The latter deeper part is expressed as stratification of 32 thin layers with a constant thickness of 0.1 km. The unknown parameters to be determined by this inversion are the thicknesses and S-wave velocities of these 35 layers. We fixed the P-wave velocities and densities as the initial model. We ignored Q values as noted above. In this inversion step, we did not use the average seafloor depth but adopted the actual depths at each grid point, because the water thickness affects the dispersion curves (Figure S1). We iterated the inversion 30 times. The top three layers were changed in both thicknesses and S-wave velocity, although the bottom layers remained nearly the same when the thickness or S-wave velocity was changed. An example of the inversion is shown in (Figure S8).

We calculated the RMS data residual (RMS′) as

$$\mathrm{RMS}' = \sqrt{\frac{|\boldsymbol{c}^{\mathrm{obs}} - \boldsymbol{c}^{\mathrm{syn}}|^2}{Q}}, \tag{15}$$

where Q is the number of horizontal grids. The RMS′ improved from 3.5×10^{-1} km/s in the initial 1-D model to 7.2×10^{-3} km/s in the final 3-D model.

The red, orange, and green regions in Figure 8, reflect layer 1, layer 2, and layer 3, respectively. The thickness of layer 1 varied from ~0.25 to ~0.55 km, which suggests that the variation is approximately 40%. The degree of thickness perturbation in layer 2 (layer 3) was generally less than 20% (10%). The variation in S-wave velocity in layers 2 and 3 was generally less than 10%.

The area with the shallower acoustic basement exists at the northern to the central regions, where seafloor depth is shallow (Figure 9a).

The S-wave velocity of the blue region in Figure 8 is consistent with that of the crust. We plotted the topography of the acoustic basement as the top of layer 3 and that of the upper crust where the S-wave velocities are larger than 3.2 km/s (e.g., Koketsu et al., 2012) in Figures 8 and 9. The topography of the upper crust has more complex topography than that between the other layers (Figure 9b). This is consistent with 2-D P-wave velocity structures (Tsuru et al., 2002; Mochizuki et al., 2008). Notably, this complexity was more evident in the southern region. To test the robustness of this feature, we repeated the same inversion analysis using different initial models with varying depths for the crust top. All of the experiment results indicated similar complexities in the northern region, which suggests this feature does not depend on initial models (Figure S9). The RMS' was improved to 9.6×10^{-3} km/s from the initial model 2 and to 1.6×10^{-2} km/s from the initial model 3.

7 Comparison with previous P-wave velocity structures

As shown by the orange and green regions in Figure 8, our S-wave velocity increased sharply from layer 2 to layer 3 in both the 1-D and 3-D structures at a depth of about 4 km, which is considered to be the acoustic basement. Tsuru et al. (2002) and Nakahigashi et al. (2012) conducted seismic reflection and refraction surveys, respectively, the survey lines of which crossed our OBS array. Tsuru et al. (2002) identified a strong reflector at 4–5 km in depth, which has been interpreted as an erosional unconformity. The P-wave velocity of the model by Nakahigashi et al. (2012) sharply increased from ~2 km/s to ~4 km/s at a depth of ~5 km. Both features roughly agree with our results, which identify the acoustic basement at a depth of 4 km. In accordance with the geological interpretation of Takahashi et al. (2004), we interpret layer 1 and layer 2 (red to green region in Figure 8) to be sedimentary layers and layer 3 (green region in Figure 8) to be Cretaceous sediment. Note that this Cretaceous sediment is consolidated, whereas the overlying layers 1 and 2 are considered unconsolidated. The region in which the S-wave velocity is larger than 3.2 km/s (blue region in Figure 8) is considered to be the upper crust.

Considering the results of Tsuru et al. (2002), the Vp/Vs ratio of layer 1 is estimated to be 4.4 (P-wave velocity: 1.5 km/s, S-wave velocity: 0.34 km/s), and that of layer 2 is 3.2 (P-wave velocity: 2.7 km/s, S-wave velocity: 0.84 km/s). The Vp/Vs ratio of layer 3, at the top of the acoustic basement, is estimated to be 2.1 (P-wave velocity: 4.4 km/s, S-wave velocity: 2.1 km/s). These Vp/Vs ratios are consistent with the values of sediments. Although the P-wave and S-wave velocities were identified on the basis of different studies, the Vp/Vs ratios are roughly consistent with the scaling law of Brocher (2005) equation (9) and are typical for the seafloor sediments (e.g., Tonegawa et al., 2017).

The upper crust showed more complex topography than the sedimentary layers, which may be caused by a subducting seamount. The P-wave velocity structure model of Mochizuki et al. (2008) suggests that a seamount is subducting in the southern part of the array. Our resultant 3-D structure has more complex topography in the southern region than that in the northern region (Figure 9). Other studies have indicated that subducting seamounts cause complexity in the crustal structure (e.g., Sun et al., 2020). Although the plate interface occurs at about 10–15 km in depth, the subducting seamounts created

numerous faults that affected the top of the overriding crust above the plate interface. Thus, the complex topography of the crustal structure in the southern region can likely be attributed to seamount subduction.

8 Potential of OBS array for investigating 3-D sedimentary structure

In this study, we revealed the high-resolution S-wave velocity structure of the sediments and the upper crust using ambient noise tomography. Conventionally, P–S converted waves at the sediment–crust boundary generated by active sources (e.g., Yamamoto et al., 2017) or passive sources (e.g., Agius et al. 2018) have been used to determine the S-wave velocity and the thickness of the sedimentary layers. Studies using active sources provide high-resolution structure but limit the resolvable region owing to their high cost. Therefore, the resolvable area is usually 2-D. On the contrary, studies using both P–S converted wave by passive sources and ambient noise can be conducted at lower cost and are feasible for revealing 3-D structures. However, they are often limited by the trade-off between the estimates of S-wave velocity and thickness. The results of the present study can be used to better constrain both parameters and to reveal the high-resolution S-wave velocity structure for the following reasons.

We used the first-higher mode in addition to the fundamental mode in this study. We demonstrate the usefulness of the first-higher mode by conducting the trans-dimensional MCMC inversion using only the fundamental mode. We again emphasize that this method imposes almost no prior constraints because we set a prior probability as a uniform distribution. We confirmed that the two top layers, layer 1 and layer 2, cannot be resolved if only the fundamental mode is used (Figure 10). This is because the first-higher mode is sensitive to both layers 1 and 2, while the fundamental mode is sensitive to the layer1 (Figure S10). Thus, the joint use of the two modes was considered to give respective constraints on these layers. In addition, the joint use of the multiple modes increased the resolution of the deeper region. When using only the fundamental mode, we obtained the maximum marginal probability at 4.6 km/s beneath the acoustic basement (Figure 10). We associate this anomalously high velocity with an artifact owing to the fixed velocity for the bottom layer, which means no constraint was added to the depths. Compared to layers 1 and 2, layer 3 is not well resolved (Figure 5). Lower-frequency data can improve the resolution of the deeper part (layer 3 or crust). However, we cannot obtain such low-frequency data below about 0.1 Hz due to the low sensitivity of the short-period sensors. For further improvement of the velocity estimation, the technique of Nakamura (Nakamura 1989; Lin et al., 2014; Berg et al., 2018) and the joint inversion of ambient noise and receiver functions (e.g., Bodin et al., 2012; Ball et al., 2014) could be feasible. However, such research is beyond the scope of this study.

Thanks to using the radial component, the first-higher mode is available. The cross-spectra calculated using the radial component have significant amplitude of the first-higher mode against those using vertical component, which is consistent with previous studies whose target region also has thick sediments beneath seafloor (e.g., Savage et al., 2013). We also calculated the ellipticity of Rayleigh wave particle motion, assuming our 1-D structure. The resultant ellipticity is 0.6–3.4 (0.1–0.25 Hz) for the fundamental mode and 6.5–34.2 (0.17–0.3 Hz) for the first-higher mode, respectively. This result agrees

with previous studies (e.g., Savage et al., 2013; Ma et al., 2016) in which the first-highr mode resulted in high ellipticity (horizontal to vertical amplitude ratio).

In addition, we were able to use high-frequency data (~0.25 Hz of the fundamental mode and ~0.3 Hz for the first-higher mode), aided by the dense OBS array with station intervals of about 6 km. In general, ambient noise tomography studies using offshore stations analyze the data of periods ranging from several to dozens of seconds because their station intervals are tens to hundreds of kilometers (e.g., Hable et al., 2019). Thus, the S-wave velocity structures were revealed mainly beneath the crust only. Shallow sedimentary structure would not be recovered by such sparse networks owing to the lower signal-to-noise ratio of the high-frequency data. Super dense arrays with station intervals of about 500 m have been deployed in oil industrial fields (Bussat and Kugler, 2011; Mordret et al., 2013; 2014); however, the development of such an array for a broader region remains challenging. The present study demonstrates that short-period OBS arrays with station intervals of 6 km deployed portably for less than one month are capable of resolving fine-scale sedimentary structure above the acoustic basement at ~0.1–1.0 km vertically and ~10 km horizontally.

Such a high-resolution S-wave velocity structure of seafloor sediments will enhance seismic waveform modeling of body waves at high frequencies, at generally greater than 0.1 Hz, for studying the deeper structures (e.g., Harmon et al., 2007) or seismic source properties beneath the ocean (e.g., Nakano et al., 2015; Takemura et al., 2020). This is because the velocity contrast across the acoustic basement strongly affects the waveform amplitude. Studies using short-period OBSs generally use only extracted information of the phase arrivals such as travel time and amplitude polarity. However, our results prove the potential to use OBS waveform records directly for studies on velocity structures and earthquake source mechanisms with higher spatio–temporal resolution.

9 Conclusion

We derived the S-wave velocity structures of sediments and the upper crust by applying ambient seismic noise tomography using continuous seismic data of 22 or 142 days from the dense array of short-period OBSs deployed off the Ibaraki region. Our S-wave velocity model included three low-velocity layers at the top, with S-wave velocities of 0.34, 0.85, and 2.1 km/s, respectively. The top two of the three layers are considered to be sediments, and the bottom layer is considered to be Cretaceous sediment. The depth of the acoustic basement is considered to be ~4 km from the seafloor, which is consistent with previous P-wave velocity tomography by active source surveys. In addition, our model shows a complex topography of the top of the upper crust in the southern region, where subducting seamounts have been indicated by previous P-wave velocity tomography. Thus, the complex topography at the upper crust might be caused by seamount subduction producing the network of numerous fractures in the top of the overriding crust. Further, we determined that using both the fundamental and the first-higher modes increases the resolution, which is facilitated by the dense OBS array with station intervals of about 6 km. Our model will make a significant contribution to waveform modeling of OBS data.

Acknowledgments

This study is supported by JSPS KAKENHI Grant Numbers 19J20692. Trans-dimensional inversion is performed using a computer program package SEIS_FILO, available at http://doi.org/10.5281/zenodo.4150550. TA is funded by JSPS Grant number JP19K21892. Our cross-correlation functions and the final 3-D S-wave velocity structure model are available at http://doi.org/10.5281/zenodo.4719128. We thank Shinji Yoneshima for providing us with the orientations of OBS horizontal components. We are grateful to the Editor Yehuda Ben-Zion, the associate editor, and two anonymous reviewers for useful comments. We also thank Yutaka Nagaoka, Akiko Takeo, Tsuyoshi Ichimura, Kohei Fujita, Takuma Yamaguchi and Takane Hori for giving us sufficient advises.

References

Agius, M. R., Harmon, N., Rychert, C. A., Tharimena, S., and Kendall, J. M. M.: Sediment characterization at the equatorial Mid-Atlantic Ridge from P-to-S teleseismic phase conversions recorded on the PI-LAB experiment, Geophys. Res. Lett., 45, 12–244, doi: 10.1029/2018GL080565, 2018.

Aki, K.: Space and time Spectra of stationary stochastic waves, with special reference to microseisms, Bull. Earthquake Res. Inst. Univ. Tokyo, 35, 415–456, 1957.

Akuhara, T., and Mochizuki, K.: Hydrous state of the subducting Philippine Sea plate inferred from receiver function image using onshore and offshore data, J. Geophys. Res., 120, 8461–8477, 2015.

Audet, P.: Receiver functions using OBS data: Promises and limitations from numerical modelling and examples from the Cascadia Initiative, Geophys. J. Int., 205, 1740–1755, 2016.

Ball, J. S., Sheehan, A. F., Stachnik, J. C., Lin, F. C., Collins, J. A.: A Joint Monte Carlo Analysis of Seafloor Compliance, Rayleigh Wave Dispersion and Receiver Functions at Ocean Bottom Seismic Stations offshore New Zealand, Geochem., Geophys., Geosys., 15, 5051–5068, doi:10.1002/2014GC005412, 2014.

Ball, J. S., Sheehan, A. F., Stachnik, J. C., Lin, F. C., Yeck, W. L., and Collins, J. A.: Lithospheric shear velocity structure of South Island, New Zealand, from amphibious Rayleigh wave tomography, J. Geophys. Res., 121, 3686–3702, 2016.

Bao, X., Song, X., and Li, J.: High-resolution lithospheric structure beneath Mainland China from ambient noise and earthquake surface-wave tomography, Earth Planet. Sci. Lett., 417, 132–141, 2015.

Bensen, G. D., Ritzwoller, M. H., Barmin, M. P., Levshin, A. L., Lin, F., Moschetti, M. P., Shapiro, N. M., and Yang, Y.: Processing seismic ambient noise data to obtain reliable broad-band surface wave dispersion measurements, Geophys. J. Int., 169, 1239–1260, 2007.

Berg, E. M., Lin, F. C., Allam, A., Qiu, H., Shen, W., Ben-Zion, Y.: Tomography of southern California via Bayesian joint inversion of Rayleigh wave ellipticity and phase velocity from ambient noise cross-correlations, J. Geophys. Res., 123, 9933–9949, 2018.

Bodin, T., Sambridge, M., Tkalčić, H., Arroucau, P., Gallagher, K., and Rawlinson, N.: Transdimensional inversion of receiver functions and surface wave dispersion, J. Geophys. Res., 117, B02301, doi: 10.1029/2011JB008560, 2012.

Brocher, T. M.: Empirical relations between elastic wavespeeds and density in the Earth's crust, B. Seismol. Soc. Am., 95, 2081–2092, 2005.

Bussat, S., and Kugler, S.: Offshore ambient-noise surface-wave tomography above 0.1 Hz and its applications, The Leading Edge, 30, 514–524, 2011.

Calkins, J. A., Abers, G. A., Ekström, G., Creager, K. C., and Rondenay, S.: Shallow structure of the Cascadia subduction zone beneath western Washington from spectral ambient noise correlation, J. Geophys. Res., 116, B07302, doi: 10.1029/2010JB007657, 2011.

Corela, C., Silveira, G., Matias, L., Schimmel, M., and Geissler, W. H.: Ambient seismic noise tomography of SW Iberia integrating seafloor-and land-based data, Tectonophysics, 700, 131–149, 2017.

Efron, B.: Bootstrap methods: another look at the jackknife, In Breakthroughs in statistics, Springer, New York, NY., 569–593, 1992.

Ekström, G., Abers, G. A., and Webb, S. C.: Determination of surface-wave phase velocities across USArray from noise and Aki's spectral formulation, Geophys. Res. Lett., 36, L18301, doi: 10.1029/2009GL039131, 2009.

Green, P. J.: Reversible jump Markov chain Monte Carlo computation and Bayesian model determination, Biometrika, 82, 711–732, 1995.

Hable, S., Sigloch, K., Stutzmann, E., Kiselev, S., and Barruol, G.: Tomography of crust and lithosphere in the western Indian Ocean from noise cross-correlations of land and ocean bottom seismometers, Geophys. J. Int., 219, 924–944, 2019.

Haney, M. M., Mikesell, T. D., van Wijk, K., and Nakahara, H.: Extension of the spatial autocorrelation (SPAC) method to mixed-component correlations of surface waves, Geophys. J. Int, 191, 189–206, 2012.

Harmon, N., Forsyth, D. W., Lamm, R., and Webb, S. C.: P and S wave delays beneath intraplate volcanic ridges and gravity lineations near the East Pacific Rise, J. Geophys. Res., 112, doi: 10.1029/2006JB004392, 2007.

Herrmann, R. B.: Computer programs in seismology: An evolving tool for instruction and research, Seism. Res. Lettr., 84, 1081–1088, doi:10.1785/0220110096, 2013.

Kanazawa, T., Uehira, K., Mochizuki, M., Shinbo, T., Fujimoto, H., Noguchi, A., Kunugi, T., Shiomi, K., Aoi, S., Matsumoto, T., Sekiguchi, S., Okada, Y.: S-net project, cabled observation network for earthquakes and tsunamis, Abstract WE2B–3 presented at SubOptic 2016, Suboptic, Dubai, 18–21 Apr.

Kaneda, Y., Kawaguchi, K., Araki, E., Matsumoto, H., Nakamura, T., Kamiya, S., Ariyoshi, K., Hori, T., Baba, T., Takahashi, N.: Development and application of an advanced ocean floor network system for megathrust earthquakes and tsunamis, Seafloor observatories, In: Favali, P. et al. (eds.), Springer Praxis Books, 643–663, doi:10.1007/978-3-642-11374-1_25, 2015.

Levshin, A. L., Yanovskaya, T. B., Lander, A. V., Bukchin, B. G., Barmin, M. P., Ratnikova, L. I., Its, E. N.: Seismic Surface Waves in a Laterally Inhomogeneous Earth, ed. Keilis-Borok, V.I., Kluwer, Norwell, Mass, 1989.

Koketsu K, Miyake H, Suzuki H.: Japan Integrated Velocity Structure Model Version 1, Proc 15th World Conf Earthq. Eng., 1–4, 2012.

Lin, F. C., Ritzwoller, M. H., Shapiro, N. M.: Is ambient noise tomography across ocean basins possible?, Geophys. Res. Lett., 33, L14304, doi:10.1029/2006GL026610, 2006.

Lin, F. C., Moschetti, M. P., Ritzwoller, M. H.: Surface wave tomography of the western United States from ambient seismic noise: Rayleigh and Love wave phase velocity maps, Geophys. J. Int., 173, 281–298, 2008.

Lin, F. C., Tsai, V. C., Schmandt, B.: 3-D crustal structure of the western United States: application of Rayleigh-wave ellipticity extracted from noise cross-correlations, Geophys. J. Int., 198, 656–670, 2014.

Lin, P. Y. P., Gaherty, J. B., Jin, G., Collins, J. A., Lizarralde, D., Evans, R. L., and Hirth, G.: High-resolution seismic constraints on flow dynamics in the oceanic asthenosphere, Nature, 535, 538–541, 2016.

Ma, Y., Clayton, R. W., Li, D.: Higher-mode ambient-noise Rayleigh waves in sedimentary basins, Geophys. J. Int., 206, 1634–1644, 2016.

Matsumura, S.: Discrimination of a preparatory stage leading to M7 characteristic earthquakes off Ibaraki Prefecture, Japan, J. Geophys. Res., 115, 2010.

Mochizuki, K., Yamada, T., Shinohara, M., Yamanaka, Y., and Kanazawa, T.: Weak interplate coupling by seamounts and repeating M~ 7 earthquakes, Science, 321, 1194–1197, 2008.

Mordret, A., Landès, M., Shapiro, N. M., Singh, S. C., Roux, P., and Barkved, O. I.: Near-surface study at the Valhall oil field from ambient noise surface wave tomography, Geophys. J. Int., 193, 1627–1643, 2013.

Mordret, A., Landès, M., Shapiro, N. M., Singh, S. C., and Roux, P.: Ambient noise surface wave tomography to determine the shallow shear velocity structure at Valhall: depth inversion with a Neighbourhood Algorithm, Geophys. J. Int., 198, 1514–1525, 2014.

Nagaoka, Y., Nishida, K., Aoki, Y., Takeo, M., and Ohminato, T.: Seismic imaging of magma chamber beneath an active volcano, Earth Planet. Sci. Lett., 333, 1–8, 2012.

Nakahigashi, K., Shinohara, M., Mochizuki, K., Yamada, T., Hino, R., Sato, T., Uehira, K., Ito, Y., Murai, Y., and Kanazawa, T.: P-wave velocity structure in the southernmost source region of the 2011 Tohoku earthquakes, off the Boso Peninsula, deduced by an ocean bottom seismographic survey, Earth Planets Space, 64, 1149–1156, 2012.

Nakamura, Y.: A method for dynamic characteristics estimation of subsurface using microtremor on the ground surface, Quaterly Report Railway Tech. Res. Inst., 30, 25–30., 1989.

Nakatani, Y., Mochizuki, K., Shinohara, M., Yamada, T., Hino, R., Ito, Y., Murai, Y., and Sato, T.: Changes in seismicity before and after the 2011 Tohoku earthquake around its southern limit revealed by dense ocean bottom seismic array data, Geophys. Res. Lett., 42, 1384–1389, 2015.

Nakano, M., Nakamura, T., & Kaneda, Y.: Hypocenters in the Nankai Trough Determined by Using Data from Both Ocean-Bottom and Land Seismic Networks and a 3D Velocity Structure Model: Implications for Seismotectonic Activity, B. Seismol. Soc. Am., 105, 1594-1605, 2015.

Nishida, K., Kawakatsu, H., and Obara, K.: Three-dimensional crustal S wave velocity structure in Japan using microseismic data recorded by Hi-net tiltmeters, J. Geophys. Res., 113, B10302, doi:10.1029/2007JB005395, 2008.

Nishida, K., Montagner, J. P., and Kawakatsu, H.: Global surface wave tomography using seismic hum, Science, 326, 112–112, 2009.

Nishikawa, T., Matsuzawa, T., Ohta, K., Uchida, N., Nishimura, T., and Ide, S.: The slow earthquake spectrum in the Japan Trench illuminated by the S-net seafloor observatories, Science, 365, 808–813, 2019.

Nishizawa, A., Kaneda, K., Watanabe, N., Oikawa, M.: Seismic structure of the subducting seamounts on the trench axis: Erimo Seamount and Daiichi-Kashima Seamount, northern and southern ends of the Japan Trench, Earth Planets Space, 61, 5–8, 2009.

Rawlinson, N., Sambridge, M.: The fast marching method: an effective tool for tomographic imaging and tracking multiple phases in complex layered media, Exploration Geophysics, 36, 341–350, 2005.

Rawlinson, N., Reading, A. M., Kennett, B. L.: Lithospheric structure of Tasmania from a novel form of teleseismic tomography, J. Geophys. Res., 111, B2, 2006.

Reeves, Z., Lekić, V., Schmerr, N., Kohler, M., and Weeraratne, D.: Lithospheric structure across the C alifornia C ontinental B orderland from receiver functions, Geochemistry, Geophysics, Geosystems, 16, 246–266, 2015.

Ruh, J. B., Sallarès, V., Ranero, C. R., Gerya, T.: Crustal deformation dynamics and stress evolution during seamount subduction: High-resolution 3-D numerical modeling, J. Geophys. Res., 121, 6880–6902, 2016.

Ryberg, T., Geissler, W. H., Jokat, W., and Pandey, S.: Uppermost mantle and crustal structure at Tristan da Cunha derived from ambient seismic noise, Earth Planet. Sci. Lett., 471, 117–124, 2017.

Saito, M.: DISPER80: A subroutine package for the calculation ofseis- mic normal-mode solutions, in Seismological Algorithms: Computational Methods and Computer Programs, Academic, London, 293–319, 1988.

Sambridge, M.: A parallel tempering algorithm for probabilistic sampling and multimodal optimization, Geophys. J. Int., 196, 357–374, 2014.

Savage, M. K., Lin, F. C., Townend, J.: Ambient noise cross-correlation observations of fundamental and higher-mode Rayleigh wave propagation governed by basement resonance, Geophys. Res. Letts., 40, doi:10.1002/grl.50678, 2013.

Saygin, E.: Seismic receiver and noise correlation based studies in Australia, Ph.D. thesis, The Australian National University, 2007.

Shapiro, N. M., Campillo, M., Stehly, L., and Ritzwoller, M. H.: High-resolution surface-wave tomography from ambient seismic noise, Science, 307, 1615–1618, 2005.

Shinohara, M., T. Yamada, K. Nakahigashi, S. Sakai, K. Mochizuki, K. Uehira, Y. Ito, R. Azuma, Y. Kaiho, T. No, H. Shiobara, R. Hino, Y. Murai, H. Yakiwara, T. Sato, Y. Machida, T. Shinbo, T. Isse, H. Miya- machi, K. Obana, N. Takahashi, S. Kodaira, Y. Kaneda, K. Hirata, S. Yoshikawa, K. Obara, T. Iwasaki, and N. Hirata, Aftershock observa- tion of the 2011 off the Pacific coast of Tohoku Earthquake by using ocean bottom seismometer network, Earth Planets Space, 63, 835–840, 2011.

Shinohara, M., Y. Machida, T. Yamada, K. Nakahigashi, T. Shinbo, K. Mochizuki, Y. Murai, R. Hino, Y. Ito, T. Sato, H. Shiobara, K. Uehira, H. Yakiwara, K. Obana, N. Takahashi, S. Kodaira, K. Hirata, H. Tsushima, and T. Iwasaki, Precise aftershock distribution of the 2011 off the Pacific coast of Tohoku Earthquake revealed by an ocean-bottom seismometer network, Earth Planets Space, 64, this issue, 1137–1148, 2012.

Shipboard Scientific Party: Leg 186 summary, Proc. Ocean Drill. Program Initial Rep., 186, 1–37, 2000.

Spica, Z. J., Nishida, K., Akuhara, T., Pétrélis, F., Shinohara, M., and Yamada, T.: Marine Sediment Characterized by Ocean-Bottom Fiber-Optic Seismology, Geophys. Res. Lett., 47, e2020GL088360, doi: 10.1029/2020GL088360, 2020.

Sun, X., Song, X., Zheng, S., Yang, Y., and Ritzwoller, M. H.: Three dimensional shear wave velocity structure of the crust and upper mantle beneath China from ambient noise surface wave tomography, Earthquake Sci., 23, 449–463, 2010.

Sun, T., Saffer, D., and Ellis, S.: Mechanical and hydrological effects of seamount subduction on megathrust stress and slip, Nature Geoscience, 13, 249–255, 2020.

Takagi, R., Nishida, K., Maeda, T., and Obara, K.: Ambient seismic noise wavefield in Japan characterized by polarization analysis of Hi-net records, Geophys. J. Int., 215, 1682–1699, 2018.

Takahashi, N., Kodaira, S., Tsuru, T., Park, J. O., Kaneda, Y., Suyehiro, K., Kinoshita, H., Abe, S., Nishino, M., and Hino, R.: Seismic structure and seismogenesis off Sanriku region, northeastern Japan, Geophys. J. Int., 159, 129–145, 2004.

Takemura, S., Yabe, S., and Emoto, K.: Modelling high-frequency seismograms at ocean bottom seismometers: effects of heterogeneous structures on source parameter estimation for small offshore earthquakes and shallow low-frequency tremors, Geophys. J. Int., 223, 1708–1723, 2020.

Takeo, A., Nishida, K., Isse, T., Kawakatsu, H., Shiobara, H., Sugioka, H., and Kanazawa, T.: Radially anisotropic structure beneath the Shikoku Basin from broadband surface wave analysis of ocean bottom seismometer records, J. Geophys. Res., 118, 2878–2892, 2013.

Tian, Y., Ritzwoller, M. H.: Improving ambient noise cross-correlations in the noisy ocean bottom environment of the Juan de Fuca plate, Geophys. J. Int., 210, 1787–1805, 2017.

Tonegawa, T., Araki, E., Kimura, T., Nakamura, T., Nakano, M., Suzuki, K.: Sporadic low-velocity volumes spatially correlate with shallow very low frequency earthquake clusters, Nature communications, 8, 1–7, 2017.

Toomey, D. R., Allen, R. M., Barclay, A. H., Bell, S. W., Bromirski, P. D., Carlson, R. L., et al.: The Cascadia Initiative: A sea change in seismological studies of subduction zones, Oceanography, 27, 138–150, 2014.

Tsuji, T., Ashi, J., Strasser, M., and Kimura, G.: Identification of the static backstop and its influence on the evolution of the accretionary prism in the Nankai Trough, Earth Planet. Sci. Lett., 431, 15–25, 2015.

Tsuru, T., Park, J. O., Miura, S., Kodaira, S., Kido, Y., and Hayashi, T.: Along-arc structural variation of the plate boundary at the Japan Trench margin: Implication of interplate coupling, J. Geophys. Res., 107, 2357, doi:10.1029/2001JB001664, 2002.

Wang, Y., Lin, F. C., Schmandt, B., and Farrell, J.: Ambient noise tomography across Mount St. Helens using a dense seismic array, J. Geophys. Res., 122, 4492–4508, 2017.

Wapenaar, K.: Retrieving the elastodynamic Green's function of an arbitrary inhomogeneous medium by cross correlation, Phys. Rev. Lett., 93, 254301, doi:10.1103/PhysRevLett.93.254301, 2004.

Weaver, R., Froment, B., and Campillo, M.: On the correlation of non-isotropically distributed ballistic scalar diffuse waves, J. Acoust. Soc. Am., 126, 1817–1826, 2009.

Yamamoto, Y., Takahashi, T., Kaiho, Y., Obana, K., Nakanishi, A., Kodaira, S., & Kaneda, Y.: Seismic structure off the Kii Peninsula, Japan, deduced from passive-and active-source seismographic data, Earth Planet. Sci. Lett., 461, 163–175, 2017.

Yang, Y., Ritzwoller, M. H., Lin, F. C., Moschetti, M. P., Shapiro, N. M.: Structure of the crust and uppermost mantle beneath the western United States revealed by ambient noise and earthquake tomography, J. Geophys. Res., 113, B12310, doi:10.1029/2008JB005833, 2008.

Zha, Y., Webb, S. C., Wei, S. S., Wiens, D. A., Blackman, D. K., Menke, W., Dunn, R. A., and Conder, J. A.: Seismological imaging of ridge–arc interaction beneath the Eastern Lau Spreading Center from OBS ambient noise tomography, Earth Planet. Sci. Lett., 408, 194–206, 2014.

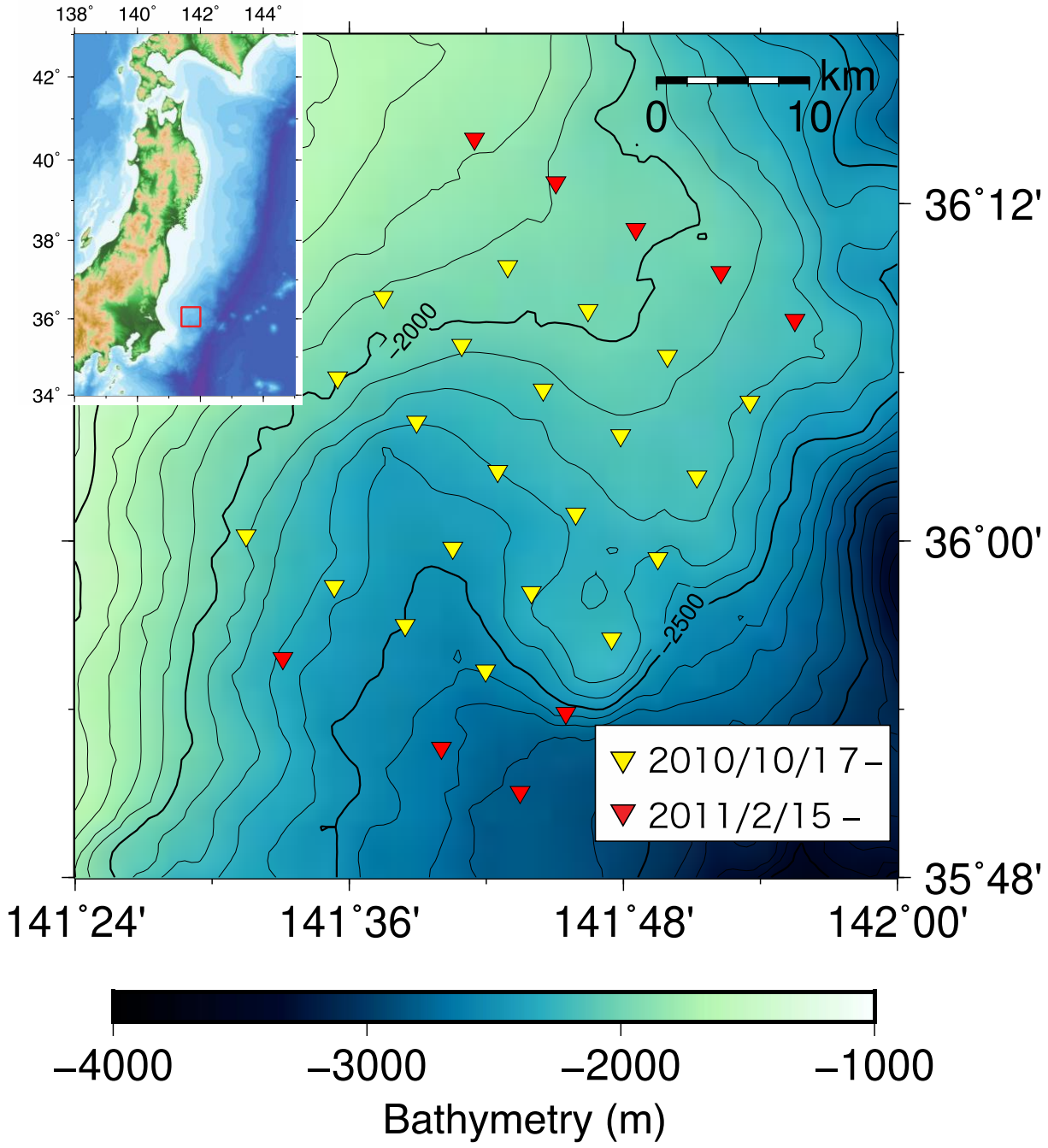

Figure 1. Stations of the OBS array in the region off Ibaraki. The station intervals are about 6 km. Yellow triangles show stations deployed on October 17, 2010, and red triangles show those deployed on February15, 201**1.**

615

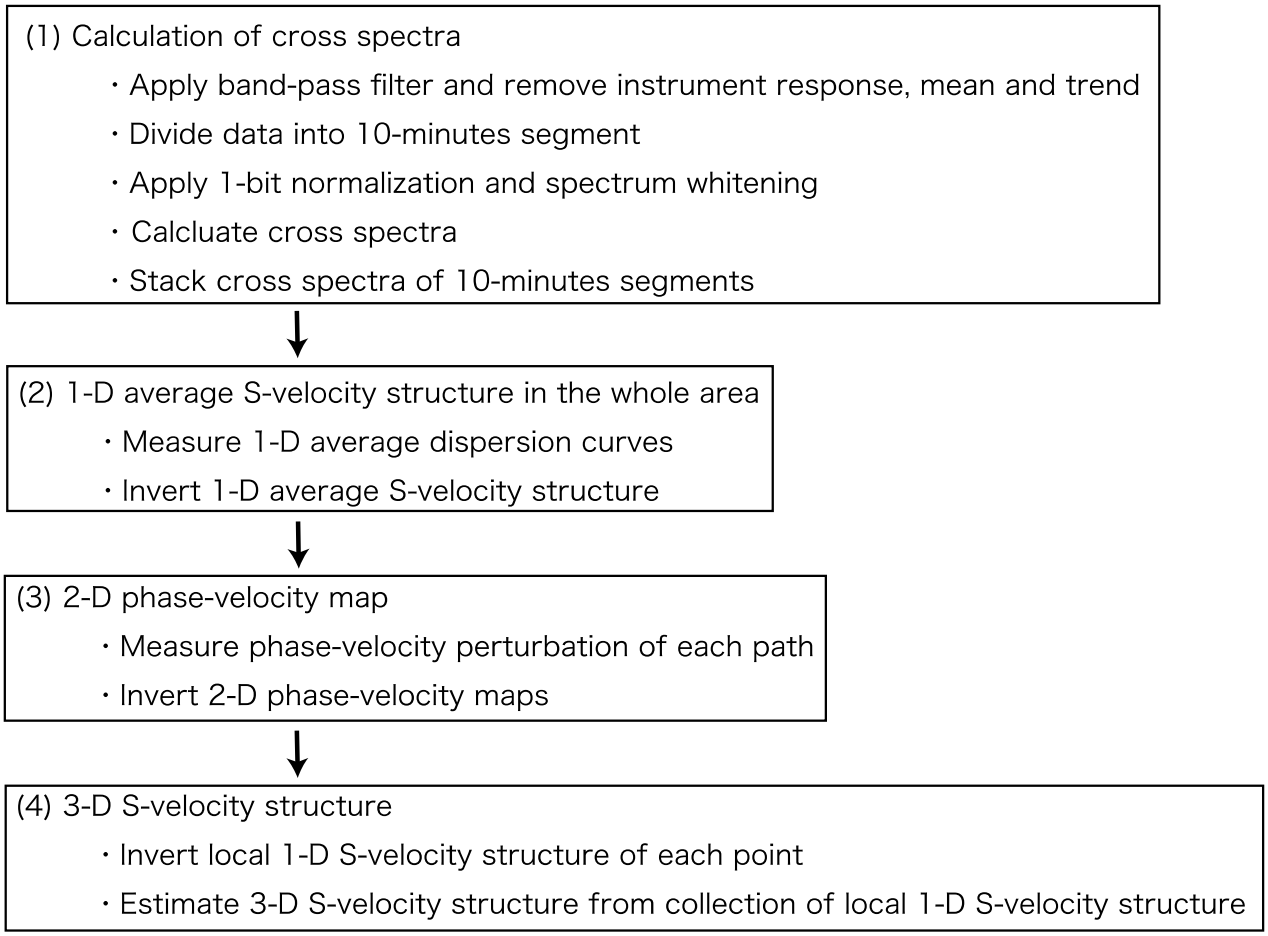

Figure 2. Schematic diagram of the analysis flow. In step (1), we calculated the cross-spectrum of each station pair. In step (2), we inferred the 1-D average S-wave velocity structure. In step (3), we inferred the 2-D phase-velocity structure. In step (4), we finally inferred the 3-D S-wave velocity structure.

620

625

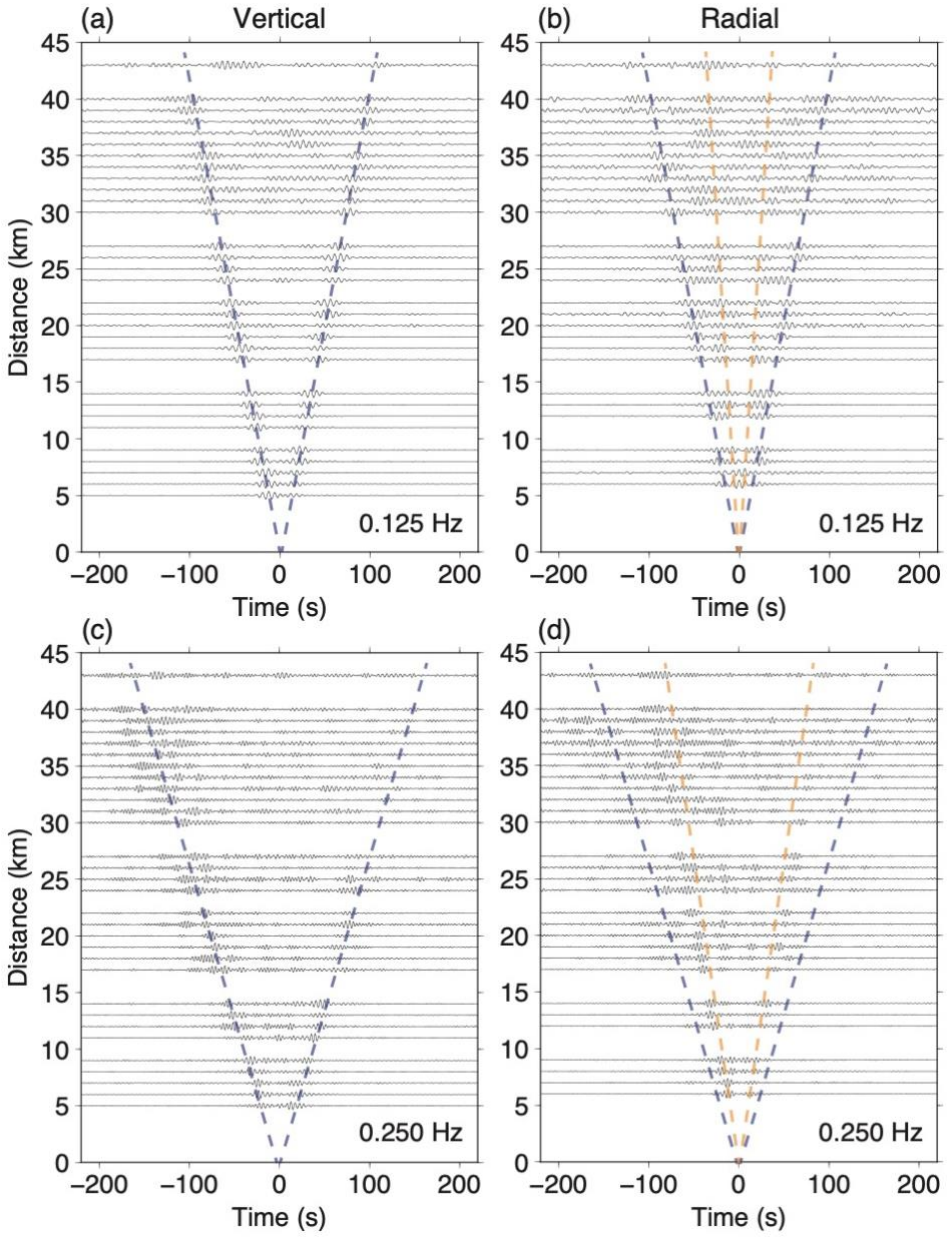

630 **Figure 3.** Stacked cross-correlation functions sorted in 1 km bins of interstation distance for all station pairs. The amplitudes are normalized by their maximum value. (a – b) Cross-correlation functions of the 0.0625–0.1875 Hz frequency range; (c – d) those of the 0.1875–0.3125 Hz frequency range. (a, c) Cross-correlation functions of the vertical components; (b, d) those of the radial components. Blue dashed lines show the fundamental-mode of Rayleigh wave and Orange dashed lines show the first-higher mode. The cross-spectra calculated using vertical component have amplitude of the fundamental mode, but those 635 using radial component have amplitude of the fundamental and the first-higher modes.

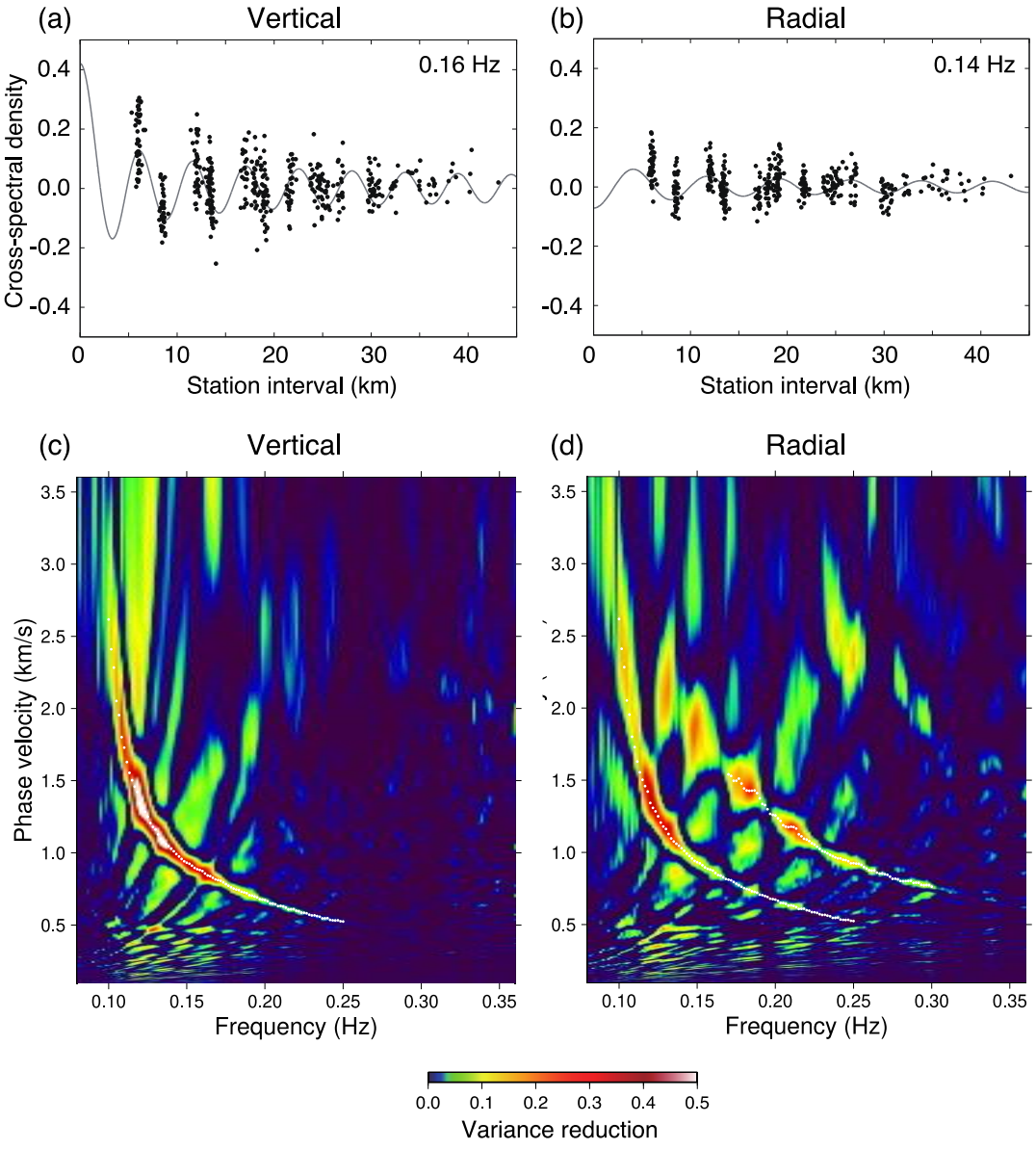

Figure 4. (a)-(b) Examples of fitting between the observed cross-spectra (solid black circles) and the synthetic curves obtained by equations (2) and (3) (gray lines). (a) Vertical component at 0.16 Hz. The assumed phase velocity is 0.87 km/s. (b) Radial component at 0.14 Hz. The assumed phase velocity is 1.05 km/s. (c – d) Variance reduction ($VR = 1 - \Delta$) between the observed cross-spectra and the synthetic curve for each component. The fundamental mode of Rayleigh wave was found in both the vertical and radial components. The first-higher mode of Rayleigh wave was clear only in the radial component. The white points show the measured 1-D average phase velocities of the fundamental and first-higher mode of Rayleigh wave.

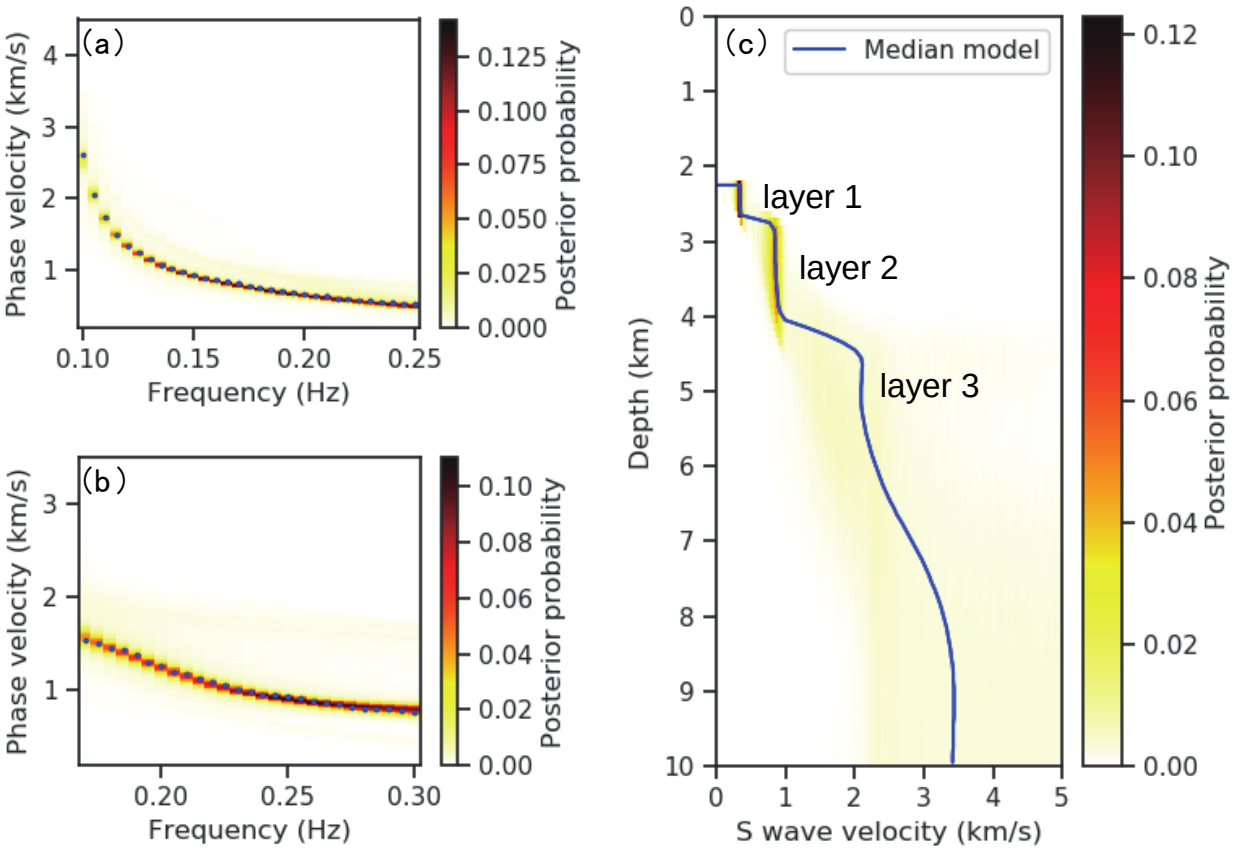

Figure 5. 1-D S-wave velocity structure inversion using both the fundamental and the first-higher modes of Rayleigh wave. (a) Phase velocity of the fundamental mode of Rayleigh wave. Blue points show the average phase velocities. The posterior probabilities were calculated for 1-D average S-wave velocity structures using the MCMC method. (b) Phase velocity of the first-higher mode of Rayleigh wave. Blue points show the 1-D average phase velocities. (c) S-wave velocity structure inferred by the MCMC method. The blue line shows the median velocity at each 0.1 km depth grid point. The layers 1 and 2 are well constrained despite the given loosely bounded uniform priors.

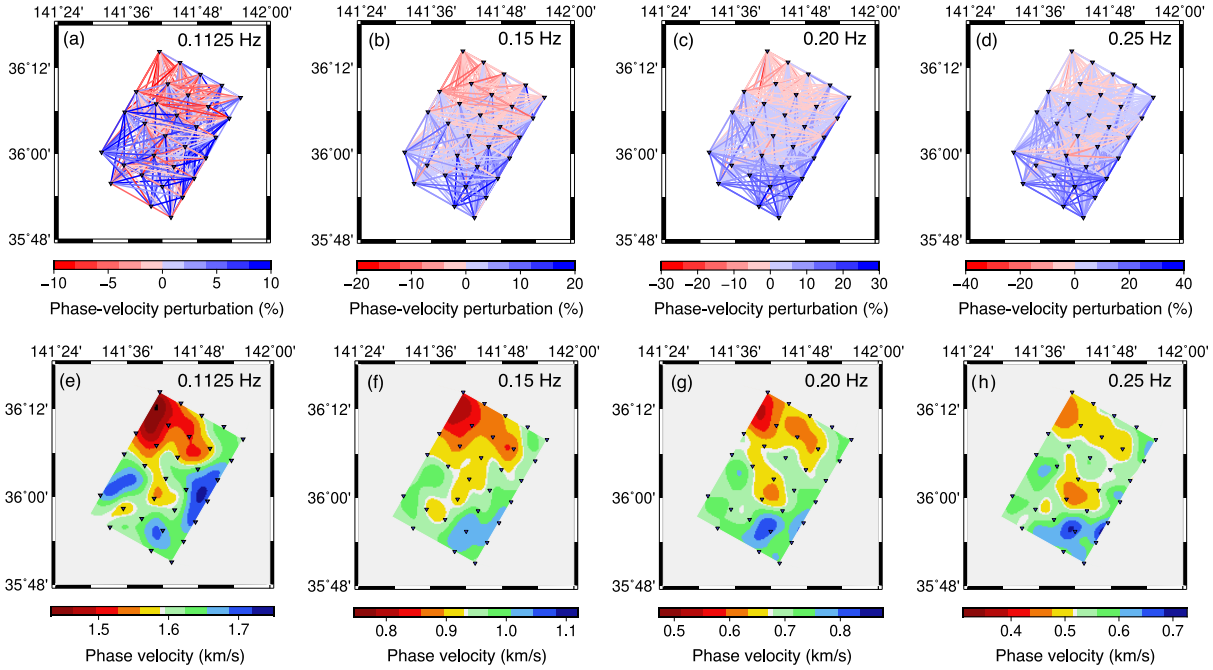

Figure 6. 2-D phase velocity inversion of the fundamental mode of Rayleigh wave. (a – d) Phase velocity perturbation of each station pair with respect to the 1-D average phase velocity in the entire area; (e – h) phase-velocity maps of the fundamental-mode of Rayleigh wave. (a, e) The case for the 0.1 - 0.125 Hz frequency range; (b, f) that for the 0.1375 - 0.1625 Hz frequency range; (c, g) that for the 0.1875 - 0.2125 Hz frequency range; (d, h) that for the 0.2375 - 0.2625 Hz frequency range. Blue triangles show the station locations. A low-velocity anomaly was located at the northern side of the array at lower frequencies, and two low-velocity anomalies were located at the northern side and central part at higher frequencies.

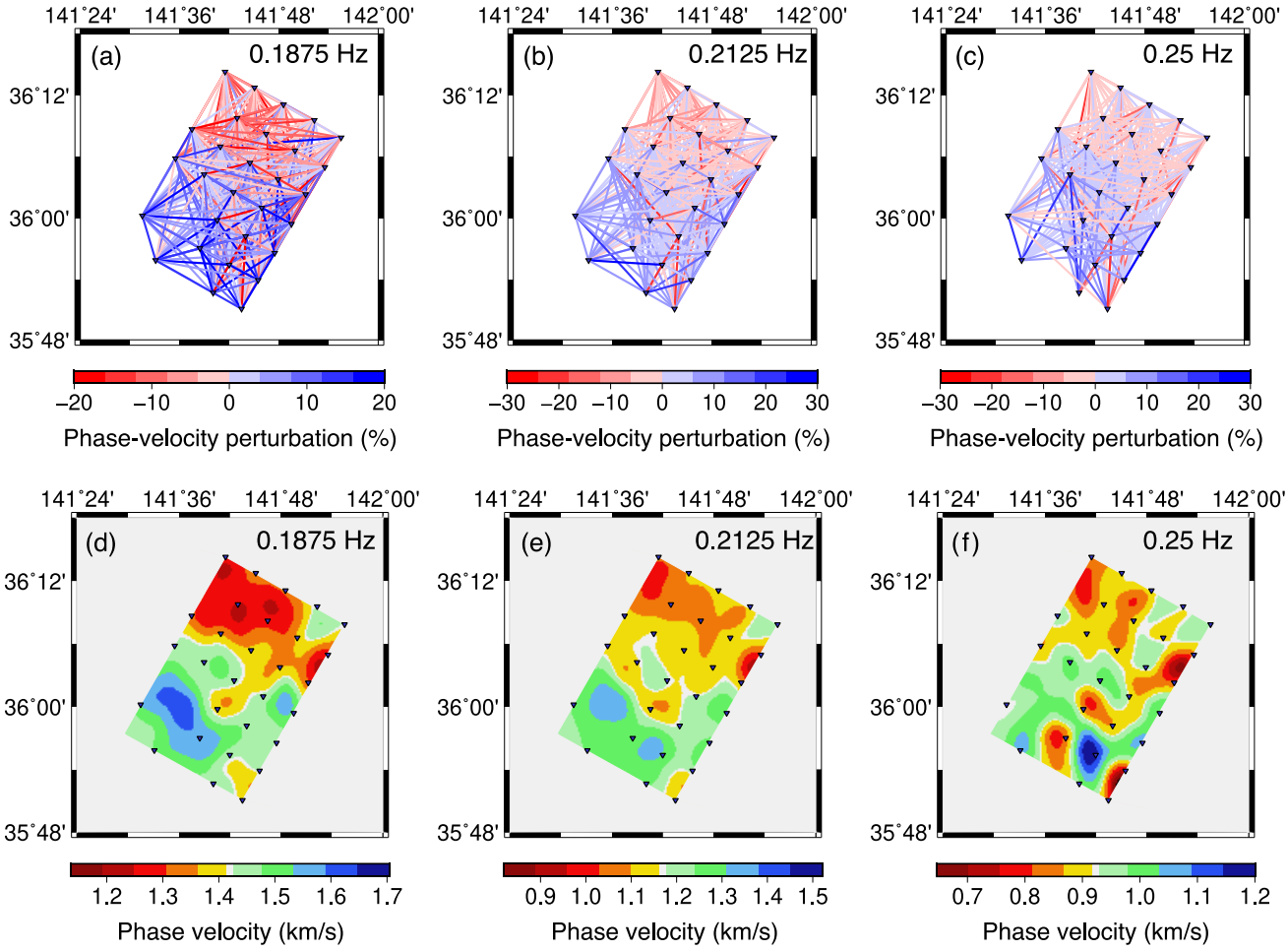

Figure 7. 2-D phase velocity inversion of the first-higher mode of Rayleigh wave. The notations are the same as those in Figure 6. (a, d) The case for the 0.175 - 0.20 Hz frequency range; (b, e) that for the 0.20 - 0.225 Hz frequency range; (c, f) that for the 0.2375 - 0.2625 Hz frequency range. Blue triangles show the station locations. A low-velocity anomaly was also located at the northern side at lower frequencies, and a low-velocity was found in the central part at higher frequencies.

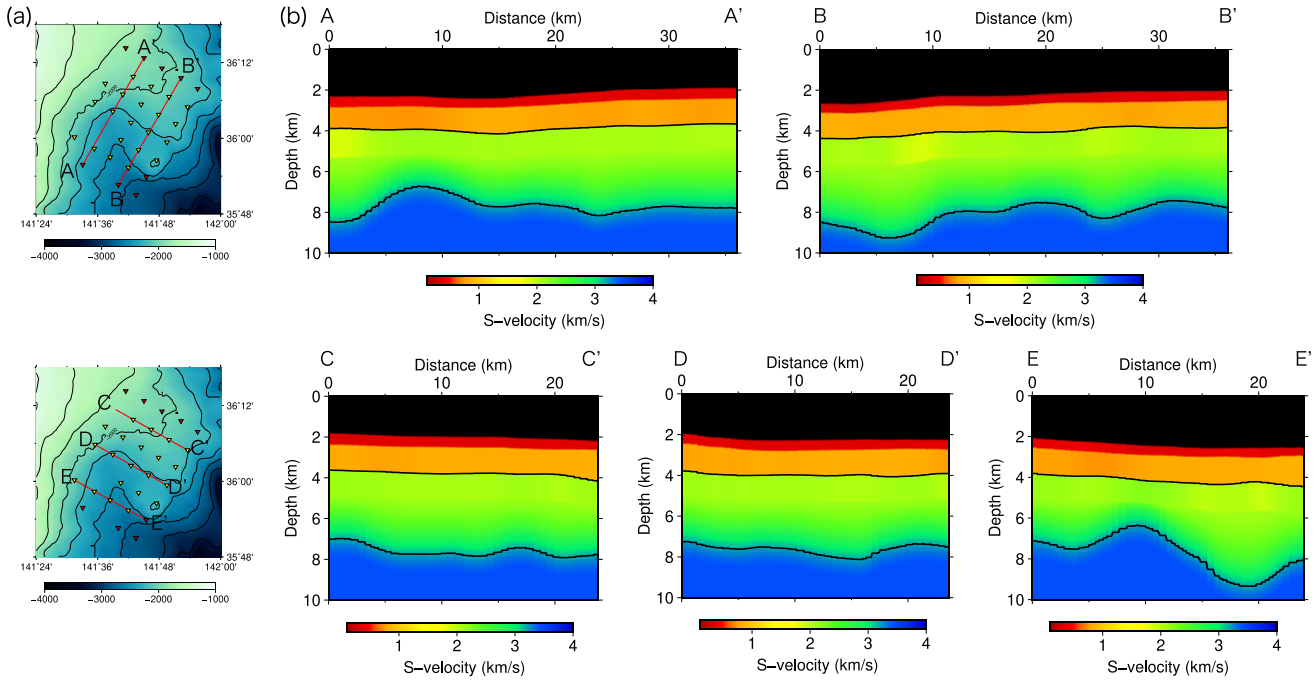

690

Figure 8. Cross-sections of 3-D S-wave velocity structure. (a) Locations of cross-sections. (b) S-wave velocities along the A–A′, B–B′, C–C′, D–D′, and E–E′ lines. The red, orange, and green regions reflect layer 1, layer 2, and layer 3, respectively. We interpret the red and orange regions to be sedimentary layers, the green region to be Cretaceous sediment, and the blue region to be the upper crust, respectively. Black lines show the depth of the acoustic basement (between orange and green regions) and the top of the upper crust (between green and blue regions).

695

700

705

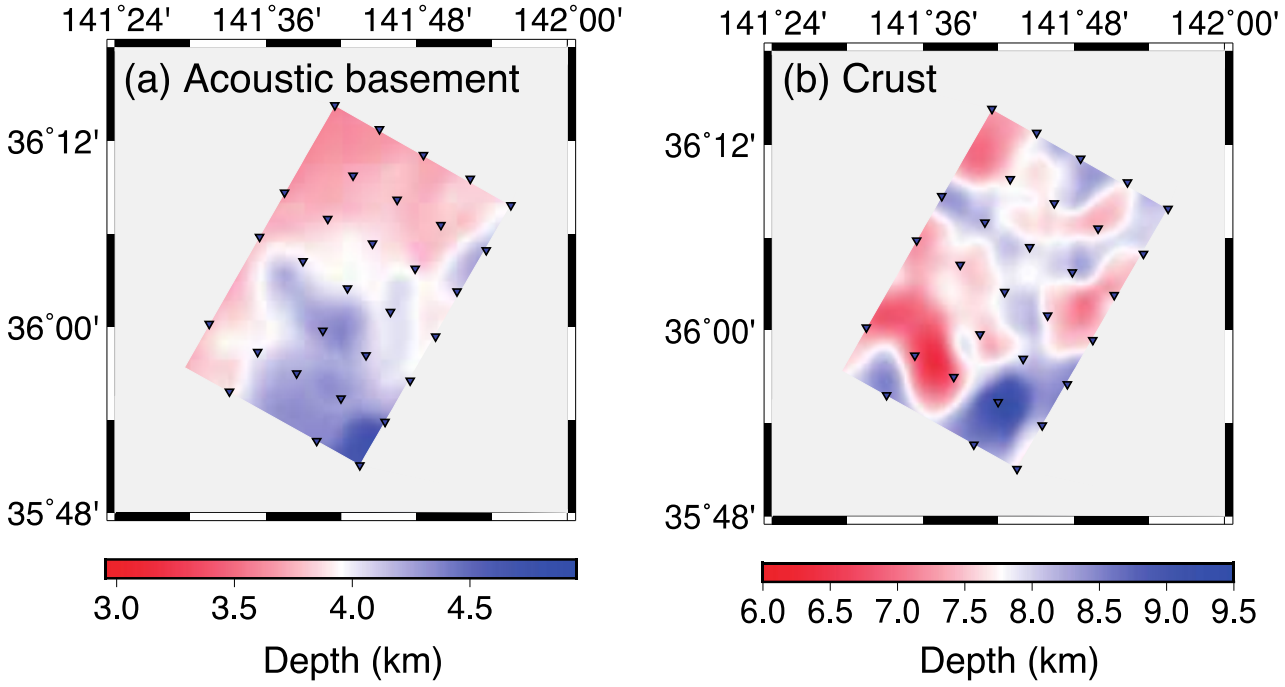

Figure 9. Depth variation of the (a) acoustic basement and (b) the top of the crust. The depth of the acoustic basement is assumed to be the bottom of layer 2, and that of the top of the crust is assumed to be the depth at which the S-wave velocity increases to greater than 3.2 km/s. The topography of the crust has more complex topography than that of the acoustic basement.

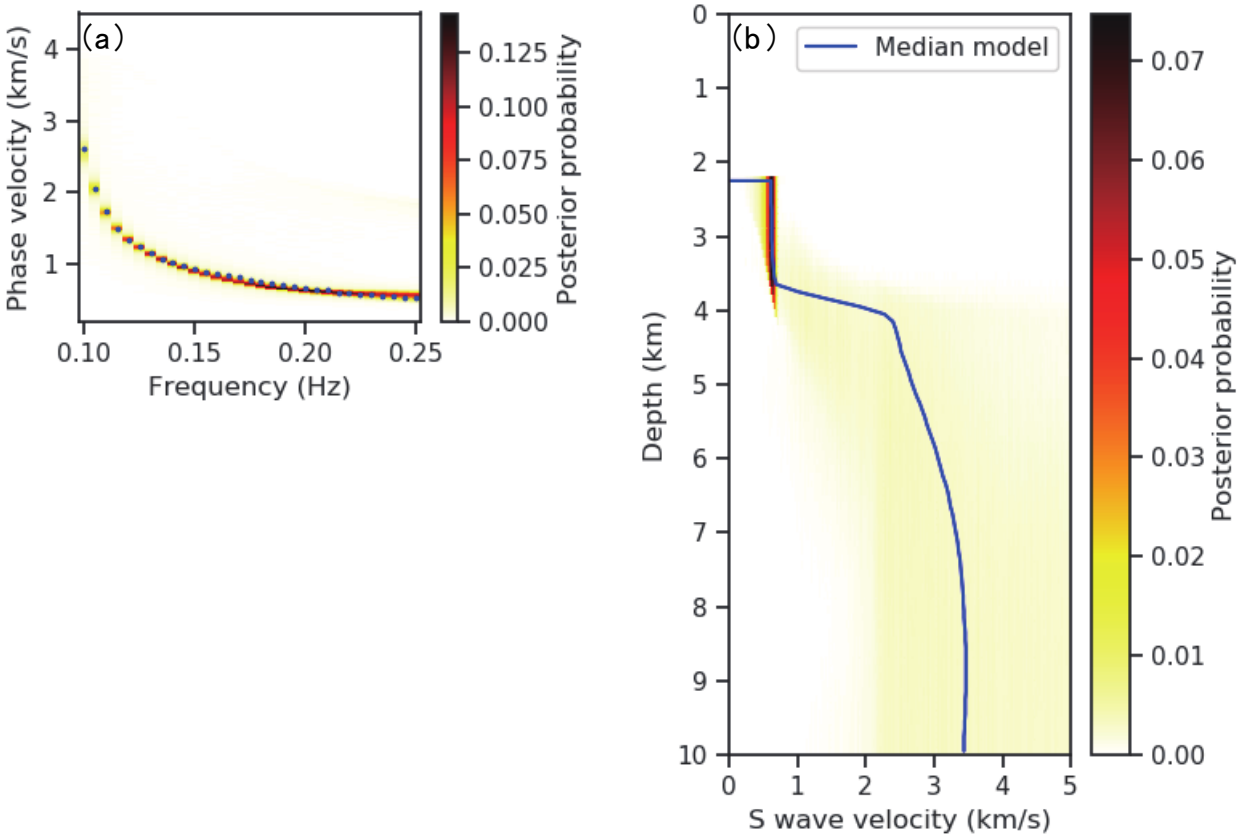

Figure 10. 1-D S-velocity structure inversion using only the fundamental mode of Rayleigh wave. The notations are the same as those in Figure 5. (a) Phase velocity of the fundamental mode of Rayleigh wave. (b) S-wave velocity structure inferred by the MCMC method. When using only the fundamental mode, we obtained the maximum marginal probability at 4.6 km/s beneath the acoustic basement. We associate this anomalously high velocity with an artifact owing to the fixed velocity for the bottom layer, which means no constraint was added to the depths.

Table 1. Search range for each station distance at the first step to measure phase-velocity perturbations. In this step, The fundamental mode first at 0.015 Hz and the first-higher mode at 0.1875 Hz are used.

Station distance	Search range for the fundamental mode	Search range for the first-higher mode
~ 10 km	-25 to 25 %	-30 to 30 %
10 ~ 15 km	-20 to 20 %	-25 to 25 %
15 ~ 20 km	-15 to 15 %	-20 to 20 %
20 km ~	-10 to 10 %	-10 to 10 %

Table 2. Search range for each station distance at the second step to measure phase-velocity perturbations. e' is the phase-velocity perturbation of the previous frequency range.

Station distance	Search range
~ 15 km	$-10 + e'$ to $10 + e'$ %
15 ~ 28 km	$-8 + e'$ to $8 + e'$ %
28 km ~	$-5 + e'$ to $5 + e'$ %